The Electrochemical Society
Advancing solid state & electrochemical science & technology

# Chemical Heterogeneity in PAN/LLZTO Composite Electrolytes by Synchrotron Imaging

View the article online for updates and enhancements.

# Chemical Heterogeneity in PAN/LLZTO Composite Electrolytes by Synchrotron Imaging

Tianze Xu,[1] Chunrun Chen,[1] Tianwei Jin,[1] Shuaifeng Lou,[1,2] Ruiwen Zhang,[1] Xianghui Xiao,[3] Xiaojing Huang,[3,z] and Yuan Yang[1,*,z]

[1]*Department of Applied Physics and Applied Mathematics, Program of Materials Science and Engineering, Columbia University, New York, New York 10027, United States of America*
[2]*MIIT Key Laboratory of Critical Materials Technology for New Energy Conversion and Storage, School of Chemistry and Chemical Engineering, Harbin Institute of Technology, Harbin 150001, People's Republic of China*
[3]*Brookhaven National Laboratory, Upton, New York, United States of America*

Solid polymer/ceramic composite electrolytes are promising for batteries due to their attractive thermal stability and mechanical properties. Chemical heterogeneity in solid composite electrolytes, such as the inhomogeneity in the ceramic phase and salt distribution at the polymer/ceramic interface, is critical to the performance of solid composite electrolytes. However, such heterogeneity has not been well understood yet. In this work, we use Synchrotron-based X-ray fluorescence imaging (XRF) and Transmission X-ray Microscope (TXM) to image nanoscale chemical heterogeneity in polyacrylamide/$Li_{7+x}La_3Zr_{2-x}Ta_xO_{12}$ (LLZTO) composite electrolytes and investigate the effects of lithium salt, salt concentration, and plasticizer. We find that LLZTO particles show strong inter- and intra-particles chemical heterogeneities, and the off-stoichiometry of Zr in an LLZTO particle is unlikely to be only balanced by Ta substitution. Moreover, statistical analysis suggests that LiI tends to accumulate at the ceramic/polymer interface at a low concentration of 5 wt%, but no such tendency was observed in samples with 10 wt% LiI. However, composite electrolytes with LiTFSI show interfacial accumulation at both 5 wt% and 10 wt%. This report provides insight into element distributions in solid composite electrolytes, and we hope further researches can shed light on the connections between chemical heterogeneity and ionic transport pathway inside.

With the rapid development of energy storage materials and devices, lithium-ion batteries (LIBs) have dominated consumer electronics and electric vehicles due to advantages such as high energy density and reasonable cost.[1,2] However, conventional LIBs utilize organic solvents with lithium salts as electrolytes, which are flammable and cause various safety issues.[3,4] In addition, liquid electrolytes are not capable of completely suppressing the growth of lithium dendrite, which promotes side reactions and potentially causes a short circuit or even an explosion of batteries.[3,4] On the other side, solid-state batteries, employing nonflammable solid electrolytes as an alternative for organic electrolytes, are attractive to address the above issues.[5]

There are two major categories of solid electrolytes: ceramic electrolytes and polymer electrolytes. The ceramic ones include oxides (e.g., Garnet-type $Li_7La_3Zr_2O_{12}$(LLZO)),[6] sulfides (e.g., $xLi_2S \cdot (100-x)P_2S_5$),[7] and phosphates (e.g., NASICON-type $Li_{1+x}Al_xGe_{2-x}(PO_4)_3$).[8] Polymer electrolytes include polyethylene oxide (PEO),[9,10] polyacrylonitrile (PAN),[11] and polyvinylidene difluoride (PVDF).[12,13] Ceramic electrolytes typically have high ionic conductivities, such as $10^{-4}$–$10^{-3}$ S cm$^{-1}$ for $Li_{7+x}La_3Zr_{2-x}Ta_xO_{12}$ (LLZTO),[14,15] and $10^{-3}$–$10^{-2}$ S cm$^{-1}$ for sulfide electrolytes.[16,17] However, ceramic electrolytes are difficult to process in a scalable way. Moreover, dendrites can also form at the grain boundary between different domains.[18] On the other side, polymer electrolytes are flexible and easy to process, but they typically have low ionic conductivities (~$10^{-5}$–$10^{-4}$ S cm$^{-1}$).[19]

To address these issues and combine the advantages of both ceramic and polymer electrolytes, ceramic/polymer composite electrolytes have drawn extensive attention recently, where ceramic electrolyte fillers are dispersed in a polymer electrolyte matrix so that the film is flexible and mechanically robust.[20] Moreover, the ceramic fillers also help plasticize the polymer matrix, amorphizing the polymer phase and thus increasing ionic conductivities.[21,22] Adding a small dose of plasticizers can also enhance the transport of

lithium ions while maintaining good mechanical properties of the electrolyte.[23] While various reports showed enhanced ionic conductivities in composite electrolytes, fundamental knowledge on chemical distribution and ion transport in composite electrolytes is still limited, especially at the nanoscale. For example, do all ceramic particle fillers have the same chemical composition? If not, the chemical heterogeneity may affect the ionic conductivity of these particles,[24] and even ionic transport at the ceramic/polymer interface. Moreover, is there any ion accumulation or depletion at the ceramic/polymer interface? Such inhomogeneity is critical to ion transport at the ceramic/polymer interface, which could affect the conductivity of the whole composite electrolyte. Classical theory points out that ion accumulation or depletion can occur at the interface due to bending of the Fermi level,[25] and salt accumulation has been occasionally reported in the literature.[26] However, a systematic analysis is still lacking.

In this report, we used the polymer-rich PAN/LLZTO composite electrolyte as a model system to understand chemical heterogeneity in composite electrolytes, which was unveiled by Synchrotron imaging with a high spatial resolution of 25–50 nm. Both X-ray fluorescence imaging (XRF) and Transmission X-ray Microscope (TXM) were used. LLZTO was chosen as the ceramic phase since it has reasonably high conductivity and is stable with lithium metal.[14,15] PAN was selected as the matrix since it is stable under the Synchrotron beam. In contrast, PEO melts quickly under Synchrotron beams. We found that LLZTO particles show significant inter- and intra- chemical heterogeneity, and the accumulation behavior of salt changed with different concentrations and types of lithium salt.

## Experimental

***Preparation of composite electrolytes and films.***—The composite electrolyte films were prepared by a solution-casting method. As the field of view of XRF is limited, LLZTO particles (MTI corporation, >99.9%) were first ball-milled down to 4–7 μm in diameter. Then PAN (Sigma-Aldrich, $M_W$ = 150,000), ball-milled LLZTO powder, and LiI (Sigma-Aldrich, 99.9%) or LiTFSI (Gotion Inc.) were mixed in N,N-Dimethylformamide (DMF,

*Electrochemical Society Member.
zE-mail: xjhuang@bnl.gov; yy2664@columbia.edu

Sigma-Aldrich, anhydrous, 99.8%) by stirring overnight. The weight ratio of lithium salt, LLZTO, and PAN was set as 1:1:10 or 0.5:1:10. In plasticized samples, succinonitrile (SN, Spectra Chemical, >99%) was also added by substituting 20 wt% of PAN to explore the effect of plasticizer. The slurries were cast on Kapton® film by a doctor blade and then dried in a vacuum oven at 60 °C overnight. The film thicknesses were controlled to be 5–8 $\mu$m.

***Electrochemical measurements.***—To measure ionic conductivities of these composite electrolytes, Au-Pd alloy was sputtered on both sides of a composite electrolyte sample to improve electrical contact. The samples were then sandwiched between stainless steel current collectors. The ionic conductivities were measured by Electrochemical Impedance Spectroscopy (EIS) with a Bio-logic VMP3 multichannel potentiostat. The frequency range was 10–1 M Hz, and the amplitude was 20 mV.

***Material characterizations.***—The morphologies and the energy dispersive spectra (EDS) of sample films were obtained by a SIGMA VP Zeiss SEM equipped with a Bruker XFlash® 6 EDS detector. X-ray diffraction patterns were measured by a PANalytical XPert3 Powder X-ray diffractometer.

***Synchrotron imaging.***—The concentrations of different elements in samples were characterized by X-ray fluorescence measurement. It was conducted at the Hard X-ray Nanoprobe beamline at NSLS-II. The incident 12 keV beam was focused to about 12 nm using a crossed pair of multilayer Laue lenses. The sample was scanned with step sizes of 50 nm. At each scan position, the emitted fluorescence signal was collected by a 3-element silicon-drift detector (Vortex ME3). The fluorescence spectra were converted to elemental maps using the PyXRF software.

The nano-tomography morphological scans of the particles in the films were conducted with the transmission X-ray microscope (TXM) at the Full-field X-ray Imaging beamline (FXI) 18-ID of the National Synchrotron Light Source II at Brookhaven National Laboratory. In a tomography scan, a sample was rotated continuously, and its projection images through TXM were continuously recorded by an optical lens coupled Andor Neo camera after X-ray being converted into visible light by a scintillator. The X-ray energy in the experiments was set to 8.7 keV. The reconstructed tomographic images have an isotropic voxel size of 39 nm. Thanks to the high scan speed of the TXM at FXI, one tomography scan could be done in half a minute, and this largely reduced the sample motion issue induced by the X-ray radiation damages on the samples.

***Data processing.***—The fluorescence spectrum collected at each scan point was fitted to identify the element types and their relative quantities from the peak locations and intensities, respectively. The obtained elemental maps were then compared with fluorescence measurements at the same experimental condition from a reference specimen with a known density. The elemental maps can quantitatively be converted to density distributions. They were processed by MATLAB and Amira-Avizo to identify particle surfaces, obtain concentration distribution, and perform correlation analysis. More details can be found in supporting notes 1–4.

## Results and Discussion

***Material characterizations of as-prepared composite electrolytes.***—To better understand how various factors (e.g., polymer electrolyte compositions, volumetric fractions of ceramic particles) affect the chemical heterogeneity in solid composite electrolytes, we prepared composite electrolytes with different salts, salt concentrations, ceramic filler fractions, and amounts of plasticizer. The exact compositions are shown in Table I. We explored two different salts (LiI and LiTFSI) and two different salt concentrations (5 wt% and 10 wt% of PAN). Besides pure PAN, we also prepared samples with SN inside, a common plasticizer in polymer electrolytes, and the

**Table I. The Composition of Lithium Salt–LLZTO–PAN–SN Samples.**

| Sample No. | Lithium salt | Composition (weight ratio) | | | |
|---|---|---|---|---|---|
| | | Lithium salt | LLZTO | PAN | SN |
| 1 | LiI | 0.5 | 1 | 10 | 0 |
| 2 | LiI | 1 | 1 | 10 | 0 |
| 3 | LiI | 0.5 | 1 | 8 | 2 |
| 4 | LiI | 1 | 1 | 8 | 2 |
| 5 | LiTFSI | 0.5 | 1 | 10 | 0 |
| 6 | LiTFSI | 1 | 1 | 10 | 0 |

amount was controlled to be 25 wt% of PAN. The reason to study the effects of SN is that it can help dissociate salts and enhance the ionic conductivity of polymer electrolytes.[21,22] Therefore, it may affect the salt distribution at the electrode/electrolyte interface.

These composite electrolyte films have similar morphologies, and Sample 2 is selected as a representative sample (Fig. 1). Figures 1a and 1b are SEM images of the top view and the cross-sectional view of the film, respectively. These figures show that LLZTO particles are well dispersed in the polymer matrix, and the polymer electrolyte thickness is typically 5–10 $\mu$m. Additional top view and cross-section images of other samples show similar morphology, which can be found in Figs. S1 and S2 (available online at stacks.iop.org/JES/168/110522/mmedia). Moreover, we also noted that, as the film thickness is close to the size of particles, the polymer electrolyte near an LLZTO particle is thicker. The effect of this phenomenon on the interpretation of imaging results will be discussed in the next section.

We further measured the temperature-dependent conductivities of these composite electrolyte films, as presented in Fig. 1c, which are similar to values reported in literature.[27] At 30 °C, the conductivities of sample 1 (5 wt% LiI) and sample 2 (10 wt% LiI) are $5.3 \times 10^{-8}$ and $7.1 \times 10^{-7}$ S cm$^{-1}$, and they increase to $1.2 \times 10^{-6}$ and $8.3 \times 10^{-6}$ S cm$^{-1}$ at 70 °C, respectively. The addition of ~25 wt% SN plasticizer helps increase the conductivity by a factor of 2–5. The conductivities of sample 3 (5 wt% LiI, with SN) and sample 4 (10 wt% LiI, with SN) reach $1.6 \times 10^{-7}$ and $3.5 \times 10^{-6}$ S cm$^{-1}$ at 30 °C, which further increase to $3.1 \times 10^{-6}$ and $1.5 \times 10^{-5}$ S cm$^{-1}$ at 70 °C, respectively. The increase of conductivity after adding SN could be attributed to the enhancement of chain mobility of PAN, which reduces the crystallinity of the polymer phase.[28,29] Moreover, SN has a high polarity that helps dissolve lithium salts and increases the concentration of the free charge carrier.[28,29] However, samples with LiTFSI have relatively lower conductivities. Even at 70 °C, the conductivities of sample 5 (5 wt% LiTFSI) and sample 6 (10 wt% LiTFSI) are only $3.1 \times 10^{-7}$ and $1.3 \times 10^{-7}$ S cm$^{-1}$, respectively, which are much lower than samples 1–4.

***Chemical heterogeneity in LLZTO particles.***—XRD was first used to examine if LLZTO powders are pure. As shown in Fig. S4, the results indicate that the LLZTO powder has no detectable impurities, so that the heterogeneity in the ceramic particles is unlikely caused by impurities inside the particles.[30]

We first studied the chemical heterogeneity in LLZTO particles by XRF imaging. The LLZTO particle has a nominal composition of Li$_{6.4}$La$_3$Zr$_{1.4}$Ta$_{0.6}$O$_{12}$, and EDS equipped in SEM gave a ratio of La: Zr: Ta = 3: 0.93: 0.4 (Fig. S3 and Table SI). On the other side, Synchrotron-based XRF results over multiple LLZTO particles show that the average ratio of La: Zr: Ta is 3: 1.83: 0.37, which does not deviate from expectation significantly. Such consistency validates that the obtained results from XRF are reasonably accurate.

XRF results first show that the chemical compositions of LLZTO particles have a high inter-particle variation. Four randomly selected particles show different La: Zr: Ta ratios of 3: 1.54: 0.41, 3: 1.80:
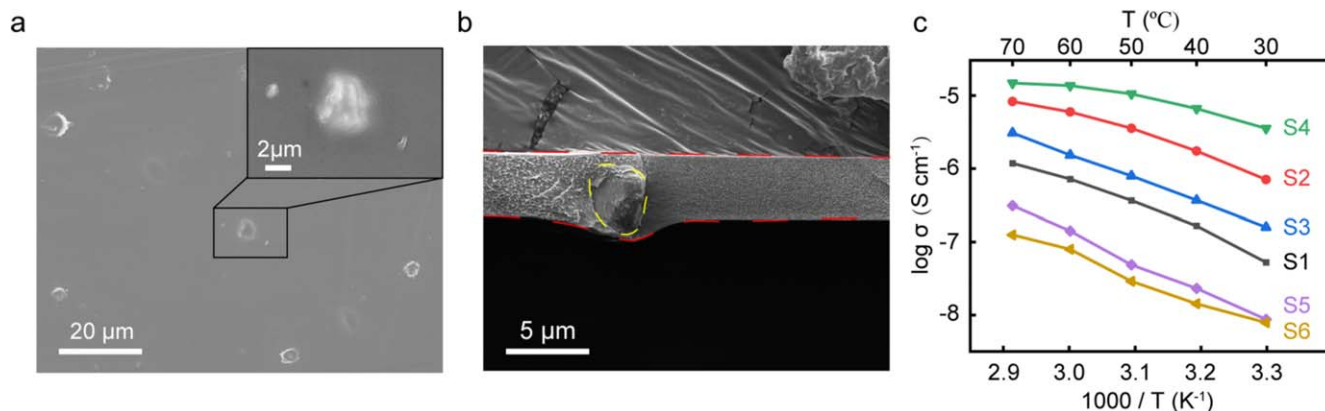
**Figure 1.** (a) and (b) SEM images of (a) the top view, and (b) the cross-sectional view of sample 2, where the red lines indicate the surfaces of films and the yellow circle indicates an LLZTO particle. (c) The temperature-dependent conductivity of composite electrolytes with different compositions, where S1–S6 corresponds to samples 1–6.

0.33, 3: 1.81: 0.36, and 3: 2.25: 0.47, respectively, indicating that there is an appreciable discrepancy from particle to particle. It suggests that the conductivity of different particles can be different, which may affect the homogeneity and pathways of ion transport in a composite electrolyte.[31]

Next, we chose one particle as an example to study intraparticle heterogeneity. First, 3D elemental distributions were obtained based on the 3D reconstruction of 2D XRF images at different angles. Then the subscripts of elements in the chemical formula of LLZTO (x, y, z in $Li_pLa_xZr_yTa_zO_q$) are calculated by converting the fluorescence signal intensity of each element to the subscript value (see supporting note 5 for more details). Figures 2a–2c show reconstructed 3D elemental distributions and representative 2D cross-sectional distributions from the 3D reconstructions. Data on more 2D distributions in this particle can be found in Fig. S5. Figures 2d–2f show the distributions of x, y, and z in the entire particle. From these images, we find that the distribution of La is approximately uniform in the whole particle, as x has a narrow distribution of 3.02 ± 0.53 in this 3D particle, with a small tail between 1 and 2.5.

In contrast, the distribution of Zr and Ta is highly heterogeneous. As shown in Figs. 2b and 2c, Zr concentrates at both the top and the bottom part of the particle, and Ta concentrates at the bottom of the particle. Further statistics of all points in the particle show that y = 1.54 ± 0.70, representing a much broader distribution of Zr compared to La. Moreover, Ta shows a multi-peak-like distribution, which concentrates at two bands of z = 0–0.25 and z = 0.4–0.75, validating the high inhomogeneity of Ta in the particle. Chemical heterogeneities in another three particles show similar results, which can be found in Figs. S6–S8.

To further confirm the large chemical variations observed, we also use 2D XRF images to study the chemical heterogeneity in LLZTO particles, which is less time-consuming. In 2D images, the intensity of an element is the product of its concentration and the sample thickness, so the chemical concentration cannot be directly evaluated from the XRF intensity. To address this issue, we plot the distribution of Zr/La and Ta/La so that the effect of thickness is canceled, which is shown in Fig. S9 (see supporting note 6 for more details). From these images, we can see that Zr/La and Ta/La are also heterogeneous. If the distribution is La is assumed to be largely uniform based on results from 3D imaging, the results suggest that Zr also show broad distributions in both particles, while both Ta distributions show multi-peak-like distributions, which are consistent with 3D imaging results.

In the classic crystal theory, Ta replaces Zr in LLZTO, creating defects to assist $Li^+$ to hop from one site to another.[32] If so, there should be a strong negative correlation between the distribution of y for Zr and z for Ta. However, as shown in Figs. 2g and 2h, the plots of y vs z show a weak positive correlation, independent of the size of

a data point. Figure 2g is based on a pixel size of $25 \times 25 \times 25\ nm^3$ ($1 \times 1 \times 1$ pixel), while in Fig. 2h, each data point corresponds to the average elemental concentration in a supercell of $100 \times 100 \times 100\ nm^3$ ($4 \times 4 \times 4$ pixels), to eliminate effects of noise and uncertainty introduced in 3D reconstruction. The corresponding correlation coefficients of y and z are 0.24 in Fig. 2g and 0.30 in Fig. 2h, respectively. Such results suggest that the off-stoichiometry of Zr is not only balanced by Ta substitution, but also the concentration variation of other elements, such as lithium and oxygen.

Sakamoto et al.[33] reported that the subcritically doped LLZTO didn't have enough $Li^+$ vacancies to stabilize the cubic phase, which led to the formation of the tetragonal phase with low conductivity in a particle. Such tetragonal phase is not detectable by XRD but can be identified by the Raman spectrum. Therefore, due to the high chemical heterogeneity in LLZTO, it is possible that some regions are subcritically doped with low conductivity and the overall conductivity of LLZTO is reduced. Moreover, different doping concentrations also result in different conductivities. For example, Goodenough et al.[34] reported that the total ionic conductivities of LLZTO measured at room temperature were 0.28, 0.73, 1.0, and 0.32 mS cm$^{-1}$ at a = 0.2, 0.4, 0.6, and 0.8 in $Li_{7-a}La_3Zr_{2-a}Ta_aO_{12}$, which echoes other reports.[35,36] Therefore, variation of z in Fig. 2c may cause conductivity heterogeneity in an LLZTO particle, and thus a composite. The effects of such heterogeneity require further analysis, which will be carried out in the future.

***Chemical heterogeneity at the LLZTO/polymer interface.***— After understanding the inhomogeneity in LLZTO particles, we further investigated the chemical inhomogeneity in the polymer electrolyte near the LLZTO/polymer interface by XRF imaging. The signal of La was used for determining the boundary of LLZTO particles since its intensity is strong and uniform inside this ceramic phase (Fig. 2a). The salt concentration in the polymer phase was measured by the intensity of iodine for LiI and sulfur for LiTFSI, respectively. We used this method because electroneutrality requires the concentration difference between anion and cation to be very small even at the nanoscale (e.g., <10 mM at a scale of 50 nm). Otherwise, the variation in electrode potential will be large enough to drive ion migration to cancel the electrical field. More analysis on this point can be found in supporting note 7. Moreover, as iodine and sulfur also distribute in the film outside the viewing field, images acquired at different rotating angles correspond to different areas. Therefore, it is difficult to reconstruct the 3D distribution of salt in the polymer matrix (Fig. S10), thus we used 2D mappings of salt concentration in the following analysis.

Figures 3a–3f show the salt concentration mapping at the LLZTO/polymer electrolyte interface in all six samples. From the images, we can clearly see the enrichment of lithium salt at
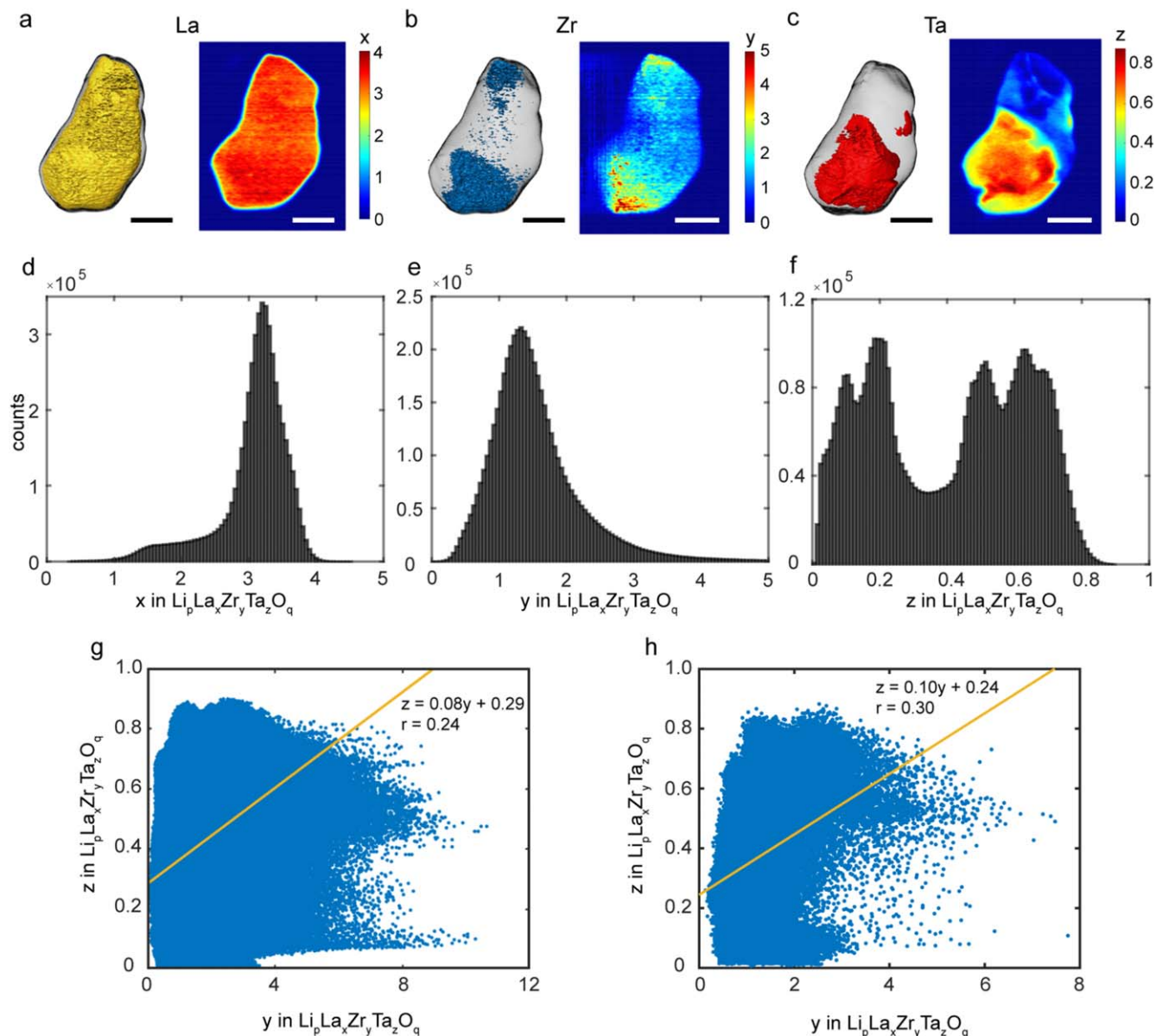
**Figure 2.** (a)–(c) Reconstructed 3D elemental distribution and representative 2D cross-sectional mappings of (a) La, (b) Zr, and (c) Ta in an LLZTO particle. x, y, z represents the subscript of La, Zr, Ta in $Li_pLa_xZr_yTa_zO_q$, respectively. The scale bars in all figures are 2 $\mu$m. (d)–(f) The distribution of (d) x, (e) y, and (f) z in the bulk of the same LLZTO particle in (a)–(c). (g) and (h) The distribution of y vs z in the bulk of the same LLZTO particle in (a)–(c), each data point corresponds to the average elemental concentration in (g) a pixel size of $25 \times 25 \times 25$ nm$^3$ ($1 \times 1 \times 1$ pixel), (h) a supercell of $100 \times 100 \times 100$ nm$^3$ ($4 \times 4 \times 4$ pixels).

the interface. We also note that the signal intensity is abnormally low on the left side of all particles. The reason is that X-ray shines from the right side, so the secondary X-ray excited from the sample is self-absorbed by the LLZTO particle, leading to a significantly reduced signal on the left side of LLZTO particles. Therefore, only signals from the right side of LLZTO particles were used for analysis, which correctly reflects salt concentration in the polymer electrolytes. Based on the 2D distribution of salt signals, we plot the 1D relation of normalized salt concentration (*c*) vs the distance from the LLZTO surface (*r*) as Figs. 3g–3i, where *c*(*r*) is the average salt concentration of all points with a distance of *r* from the LLZTO surface. We can see that *c* drops fast first and then gradually becomes flat at a value of 50%–80% of the maximum concentration at the LLTZO/PAN interface. These results suggest that salt is enriched at the LLZTO/polymer interface.

However, the higher salt concentration at the LLZTO/polymer interface could arise from other factors such as salt precipitation and

thicker film near the interface. To exclude these mechanisms, a series of experiments were conducted. First, we used XRD to exclude possible salt precipitation at the interface. XRD results of crystalline LiI powders, crystalline LiTFSI powders, the substrate of samples, and all six samples are shown in Fig. 4. All composite electrolytes share similar peaks, and all of them can be found in the substrate, which is consistent with the characteristic peaks of the Kapton® substrate and $\gamma$-Fe in the XRD stage. Moreover, major peaks of LiTFSI and LiI cannot be found in the XRD pattern of electrolyte samples. These results indicate that there is no apparent salt crystallization in these samples to cause artifacts of salt accumulation.

We then studied whether the enrichment in Fig. 3 arises from the larger film thickness at the LLZTO/polymer electrolyte interface, as observed in cross-sectional SEM images (Figs. 1b and S2). Since the concentration mapping is two-dimensional, a larger film thickness around a particle will result in a higher local intensity and thus increase apparent salt concentration at the interface. To exclude this
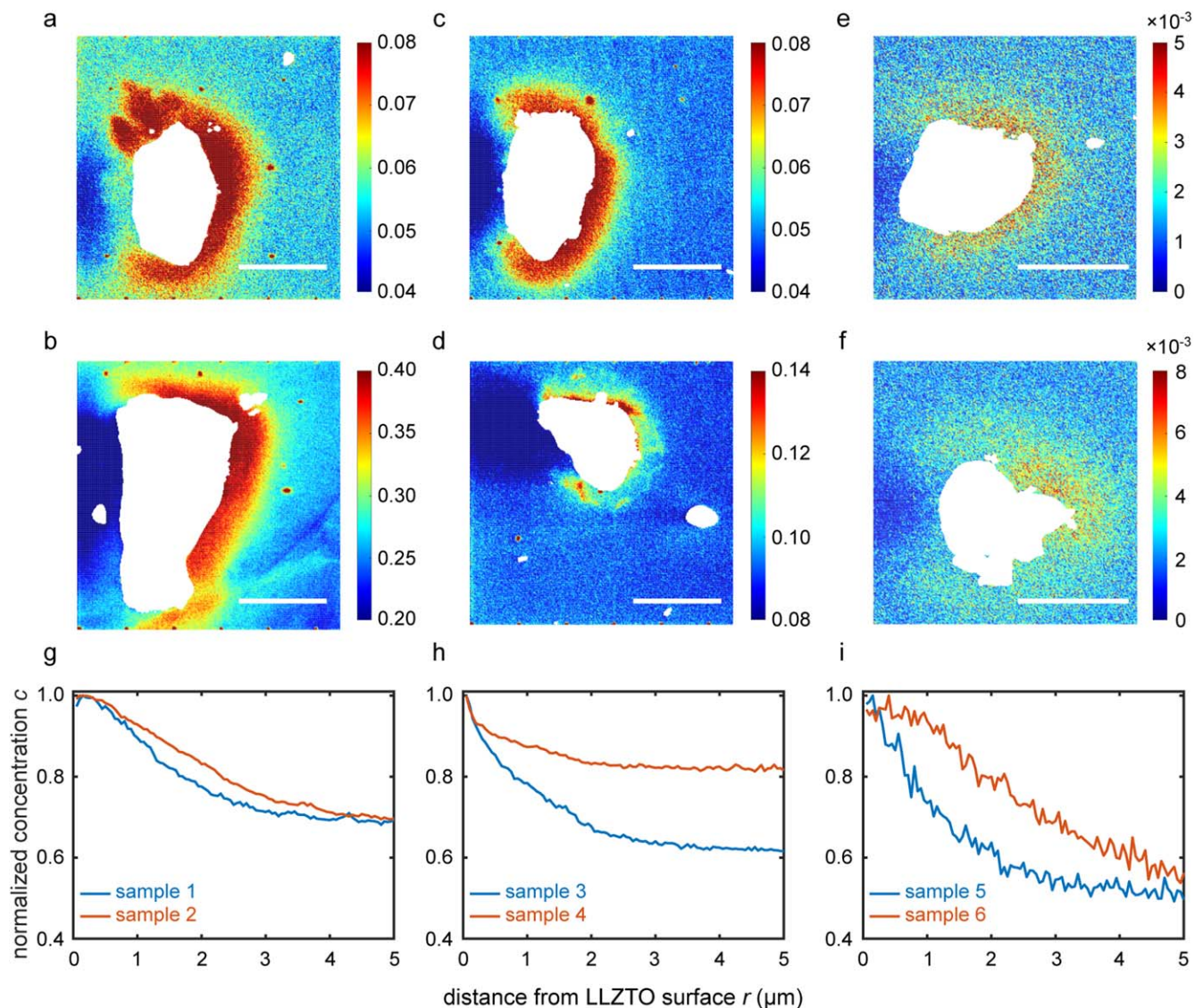
**Figure 3.** (a)–(f) 2D-summed mappings of the intensity of iodine in (a) sample 1, (b) sample 2, (c) sample 3, (d) sample 4, and 2D-summed mappings of the intensity of sulfur in (e) sample 5, and (f) sample 6. The white part in each image corresponds to an LLZTO particle, and the scale bars in all figures are 5 $\mu$m. (g)–(i) The dependence of the normalized concentration of lithium salt ($c$) on the distance from the LLZTO surface ($r$) in (g) samples 1–2, (h) samples 3–4, and (i) samples 5–6, where the maximum concentration of each sample is set as 1.

factor, we applied transmission X-ray microscopy (TXM) to estimate the variation of film thickness near the LLZTO/polymer interface. Unfortunately, TXM and XRF are at two different beamlines so that it is difficult to image the same particle by both techniques. Therefore, we performed a statistical analysis of thickness variation in multiple particles in a sample. Then we compared the ratio of the salt concentration at the interface to that in the bulk ($R_c$) and the ratio of film thickness at the interface to that in the bulk ($R_t$). If $R_c$ is larger than $R_t$, it indicates that there is still salt accumulation at the interface.

The results of all samples are summarized in Table II, and corresponding representative TXM images are shown in Fig. S11. Table II shows that in samples 1 and 3, where LiI is 5 wt%, $R_c$ are $1.39 \pm 0.13$ and $1.48 \pm 0.21$, which are apparently higher than $R_t$ of $1.19 \pm 0.07$ and $1.10 \pm 0.03$, respectively. Therefore, it is very likely that salt accumulation exists at the interface. In contrast, in samples 2 and 4, where LiI is 10 wt% of the polymer matrix, $R_c$ are $1.21 \pm 0.12$ and $1.26 \pm 0.07$, and $R_t$ are $1.21 \pm 0.06$ and $1.29 \pm 0.09$, respectively. Therefore $R_c/R_t = 1.00 \pm 0.11$ for sample 2 and $1.02 \pm 0.09$ for 4. It suggests that it is unclear if the salt enrichment in these two samples exist, since it could be a result of larger film thicknesses at the LLZTO/polymer interface. These results indicate that LiI is more likely to

accumulate at the ceramic/polymer interface at a lower concentration. On the other side, samples with LiTFSI show a different behavior on salt accumulation. As shown in Table II, $R_t$ of samples 5 and 6 stay similar to samples 1–4 as expected, but their $R_c$ are much higher than samples with LiI. As a result, $R_c/R_t = 1.58 \pm 0.25$ and $2.35 \pm 0.64$ for samples 5 and 6, respectively. These results indicate that LiTFSI accumulation exists at both low and high concentrations. The results also show that samples 3 and 4 with SN added have a similar degree of salt accumulation at the LLZTO/polymer interface as samples 1 and 2. These results indicate that the accumulation of lithium salts is not significantly affected by plasticizers.

Besides the effects of salt concentration and plasticizers, it should be noticed that $Li_2CO_3$ may form on the LLZTO surface, which has been reported to be critical to interfacial ion transport. Similarly, $Li_2CO_3$ may affect lithium salt distribution near the interface. This needs to be further studied.

**Conclusions**

In conclusion, we synthesized six PAN-LLZTO based solid composite electrolytes with different compositions and analyzed

**Table II. Concentration and thickness variations of different samples between the interface and the polymer phase.**

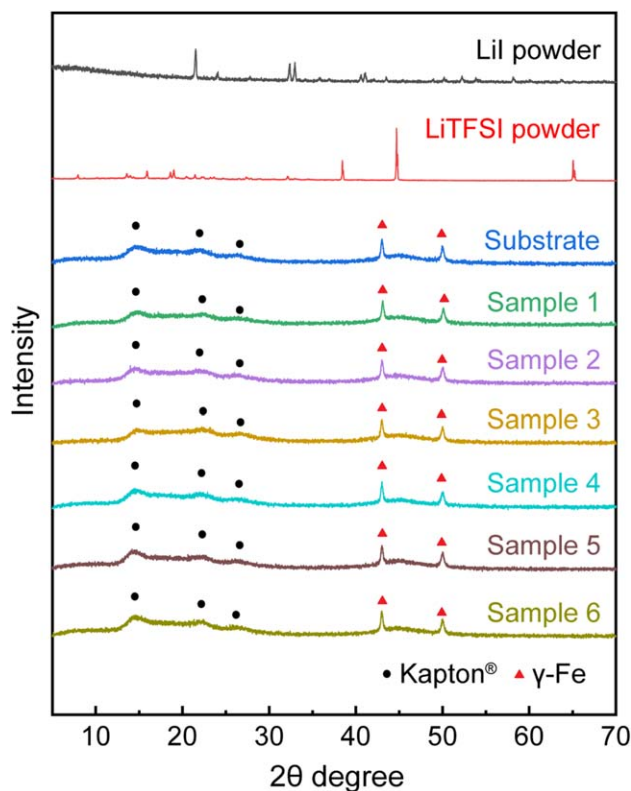| Samples | Concentration ratio ($R_c$) | Thickness ratio ($R_t$) | $R_c/R_t$ |
|---|---|---|---|
| 1 | 1.39 ± 0.13 | 1.19 ± 0.07 | 1.16 ± 0.12 |
| 2 | 1.21 ± 0.12 | 1.21 ± 0.06 | 1.00 ± 0.11 |
| 3 | 1.48 ± 0.21 | 1.10 ± 0.03 | 1.35 ± 0.19 |
| 4 | 1.26 ± 0.07 | 1.29 ± 0.09 | 1.02 ± 0.09 |
| 5 | 1.95 ± 0.29 | 1.24 ± 0.06 | 1.58 ± 0.25 |
| 6 | 2.64 ± 0.67 | 1.12 ± 0.11 | 2.35 ± 0.64 |



**Figure 4.** XRD patterns of LiTFSI powder, LiI powder, substrate, and samples 1–6. Peaks in the substrate can be assigned to Kapton® film and $\gamma$-Fe.

them by XRF to understand the distribution of various elements inside. In LLZTO particles, strong intraparticle and interparticle heterogeneity were observed. Moreover, statistics show that there is little correlation between the concentration of Zr and Ta in the same particle, indicating the off-stoichiometry of Zr is not only balanced by Ta substitution, but also the concentration variation of other elements, such as lithium and oxygen. We also found different behaviors of lithium salt accumulation for LiI and LiTFSI. While LiI is enriched at the ceramic/polymer interface only at a lower salt concentration of 5 wt%, LiTFSI accumulates in samples with salt concentrations of both 5 wt% and 10 wt%. As the heterogeneity of elements in composite electrolytes is closely related to the conduction of lithium ions, we hope further research could unveil the relationship between the element heterogeneity and the mechanism of ion conduction.

### Acknowledgments

### ORCID

Yuan Yang  https://orcid.org/0000-0003-0264-2640

### References

1. M. Armand and J. M. Tarascon, *Nature*, **451**, 652 (2008).
2. J. M. Tarascon and M. Armand, *Nature*, **414**, 359 (2001).
3. K. Xu, *Chem. Rev.*, **104**, 4303 (2004).
4. K. Xu, *Chem. Rev.*, **114**, 11503 (2014).
5. N. Kamaya, K. Homma, Y. Yamakawa, M. Hirayama, R. Kanno, M. Yonemura, T. Kamiyama, Y. Kato, S. Hama, and K. Kawamoto, *Nat. Mater.*, **10**, 682 (2011).
6. R. Murugan, V. Thangadurai, and W. Weppner, *Angew. Chem. Int. Ed.*, **46**, 7778 (2007).
7. R. Mercier, J.-P. Malugani, B. Fahys, and G. Robert, *Solid State Ionics*, **5**, 663 (1981).
8. B. E. Taylor, A. D. English, and T. Berzins, *Mater. Res. Bull.*, **12**, 171 (1977).
9. M. B. Armand, J. M. Chabagno, and M. J. Duclot, *Fast iontransport in solids: electrodes and electrolytes*, ed. P. Vashishta, JN Mundy, and G. K Shenoy (Elsevier, New York, NY) 52 (1979).
10. D. E. Fenton, *Polymer*, **14**, 589 (1973).
11. M. Watanabe, M. Kanba, H. Matsuda, K. Tsunemi, K. Mizoguchi, E. Tsuchida, and I. Shinohara, *Die Makromolekulare Chemie, Rapid Communications*, **2**, 741 (1981).
12. E. Tsuchida, H. Ohno, and K. Tsunemi, *Electrochim. Acta*, **28**, 591 (1983).
13. K. Tsunemi, H. Ohno, and E. Tsuchida, *Electrochim. Acta*, **28**, 833 (1983).
14. S. Ohta, T. Kobayashi, J. Seki, and T. Asaoka, *J. Power Sources*, **202**, 332 (2012).
15. J. L. Allen, J. Wolfenstine, E. Rangasamy, and J. Sakamoto, *J. Power Sources*, **206**, 315 (2012).
16. A. Sakuda, A. Hayashi, and M. Tatsumisago, *Sci. Rep.*, **3**, 2261 (2013).
17. J. Lau, R. H. DeBlock, D. M. Butts, D. S. Ashby, C. S. Choi, and B. S. Dunn, *Adv. Energy Mater.*, **8**, 1800933 (2018).
18. H.-K. Tian, Z. Liu, Y. Ji, L.-Q. Chen, and Y. Qi, *Chem. Mater.*, **31**, 7351 (2019).
19. J. Wan, J. Xie, X. Kong, Z. Liu, K. Liu, F. Shi, A. Pei, H. Chen, W. Chen, and J. Chen, *Nat. Nanotechnol.*, **14**, 705 (2019).
20. X. Zhang, T. Liu, S. Zhang, X. Huang, B. Xu, Y. Lin, B. Xu, L. Li, C.-W. Nan, and Y. Shen, *JACS*, **139**, 13779 (2017).
21. R. C. Agrawal and R. K. Gupta, *J. Mater. Sci.*, **34**, 1131 (1999).
22. H. Zhai, P. Xu, M. Ning, Q. Cheng, J. Mandal, and Y. Yang, *Nano Lett.*, **17**, 3182 (2017).
23. H. Al-Salih, A. Huang, C.-H. Yim, A. I. Freytag, G. R. Goward, E. Baranova, and Y. Abu-Lebdeh, *J. Electrochem. Soc.*, **167**, 070557 (2020).
24. J. Maier, *J. Electrochem. Soc.*, **134**, 1524 (1987).
25. Z. Zhang and J. T. Yates, *Chem. Rev.*, **112**, 5520 (2012).
26. C. Hu et al., *JACS*, **142**, 18035 (2020).
27. M. Forsyth, S. Jiazeng, and D. R. MacFarlane, *Electrochim. Acta*, **45**, 1249 (2000).
28. C. Wang, Q. Liu, Q. Cao, Q. Meng, and L. Yang, *Solid State Ionics*, **53–56**, 1106 (1992).
29. D. R. MacFarlane, J. Sun, P. Meakin, P. Fasoulopoulos, J. Hey, and M. Forsyth, *Electrochim. Acta*, **40**, 2131 (1995).
30. Y. Ren, T. Liu, Y. Shen, Y. Lin, and C.-W. Nan, *Journal of Materiomics*, **2**, 256 (2016).
31. H. Buschmann, S. Berendts, B. Mogwitz, and J. Janek, *J. Power Sources*, **206**, 236 (2012).
32. C. Wang et al., *Chem. Rev.*, **120**, 4257 (2020).
33. T. Thompson, J. Wolfenstine, J. L. Allen, M. Johannes, A. Huq, I. N. David, and J. Sakamoto, *J. Mater. Chem. A*, **2**, 13431 (2014).
34. Y. Li, J.-T. Han, C.-A. Wang, H. Xie, and J. B. Goodenough, *J. Mater. Chem.*, **22**, 15357 (2012).
35. Y. Wang and W. Lai, *Electrochem. Solid-State Lett.*, **15**, A68 (2015).
36. R. Inada, K. Kusakabe, T. Tanaka, S. Kudo, and Y. Sakurai, *Solid State Ionics*, **262**, 568 (2014).